Inorganic Chemistry

Article

pubs.acs.org/IC

Room-Temperature Pressure-Induced Nanostructural $CuInTe_2$ Thermoelectric Material with Low Thermal Conductivity

Atsuko Kosuga,* Kouhei Umekage, Mie Matsuzawa, Yasuhiro Sakamoto, and Ikuya Yamada

Nanoscience and Nanotechnology Research Center, Research Organization for the 21st Century, Osaka Prefecture University, Gakuencho 1-2, Sakai 599-8570, Japan

Supporting Information

ABSTRACT: A room-temperature high-pressure synthesis method is proposed as an alternative way to induce nanoscale structural disorder in the bulk thermoelectric $CuInTe_2$ matrix. This disorder stems from the coexistence of distinct domains with different degrees and geometries of disorder at Cu/In cation sites. The lattice thermal conductivity of high-pressure-treated $CuInTe_2$ is substantially less than that of hot-pressed $CuInTe_2$. The Debye−Callaway model reveals that the reduced lattice thermal conductivity is mainly attributed to disorder at the Cu/In cation sites and stacking faults, which were probably created during formation of the high-pressure-treated phases. This study demonstrates that room-temperature high-pressure synthesis can produce a radical change in the crystal structure and physical properties of conventional thermoelectric materials.

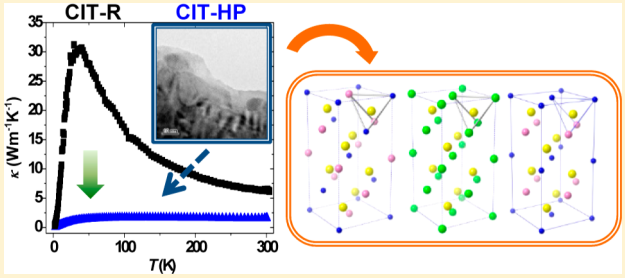

INTRODUCTION

In recent years, bulk nanostructured materials have attracted increasing interest in material science, not only because of their intriguing physical properties,[1−3] but also from a practical perspective because of the cost-effectiveness and scalability of such materials for various applications. In particular, there has been significant improvement in the performance of bulk nanostructured thermoelectric materials for large-scale waste-heat recovery applications. The conversion efficiency of a thermoelectric material is governed by the following dimensionless figure of merit: $ZT = S^2T/\rho\kappa$, where S is the Seebeck coefficient, ρ is the electrical resistivity, T is the absolute temperature, and κ is the thermal conductivity.[4,5] Enhancement of ZT can be achieved through nanostructuring, where the nanostructures impede much of the heat flow in the system while leaving the charge carrier largely unaffected, which results in significant reduction of κ. Recent extensive studies have achieved ZT values greater than 1, mainly in PbTe systems such as La-doped PbTe−Ag_2Te,[6] PbTe−PbS,[7] and $Pb_{1-x}Sn_xTe$−PbS.[8] Most of these bulk nanostructured materials were prepared by metallurgical approaches, such as precipitation, nucleation and growth, spinodal decomposition, eutectic, and matrix encapsulation methods. These reactions are controlled by heat treatment, and there are very few reports investigating other approaches.[9,10]

Here, we show an alternative route to fabricate nanostructured thermoelectric materials by room-temperature high-pressure synthesis. Chalcopyrite and related compounds exhibit pressure-induced structural modification.[11−13] Structural modification of $CuInTe_2$ occurs at 3.6 GPa with transformation into the cation site disordered *Cmcm* (d-*Cmcm*) structure.[11] In this study, we discovered that the high-pressure phase of $CuInTe_2$ is not stable at ambient pressure. Moreover, it cannot return to the pre-pressure-treated chalcopyrite phase after application of pressure of 5 GPa and subsequent pressure decrease to ambient pressure. Instead, a new phase with nanoscale structural disorder is formed, leading to a drastic reduction in κ. In the past few years, $CuInTe_2$ and its related compounds with the chalcopyrite structure have been identified as potential thermoelectric materials,[14−18] except they have high κ.[19] Hence, potential improvement of ZT is possible through the reduction of κ using room-temperature high-pressure synthesis.

From a different perspective, this work should open up a new field of high-pressure chemistry. Many studies related to high-pressure synthesis have focused on obtaining novel high-pressure phases by high-pressure and high-temperature synthesis,[20,21] and the materials obtained in this way are considered to be kinetically stable at ambient pressure. Other studies have focused on rapidly tuning a material's interaction parameters under high pressure at room temperature rather than performing chemical tuning to enhance the search for materials with improved properties.[22,23] In such cases, the stability at ambient pressure has not been analyzed. This work is the first report focusing on samples that have experienced pressure-induced structural modification and whose crystal structure and physical properties are different from those of either the pre-pressure-treated or high-pressure phase. Thus, a room-temperature high-pressure method could be a novel method to produce conventional inorganic materials with unusual and useful properties.

Received: March 24, 2014
Published: June 10, 2014

   dx.doi.org/10.1021/ic500688d | *Inorg. Chem.* 2014, 53, 6844−6849

EXPERIMENTAL SECTION

$CuInTe_2$ powder was prepared by melting a stoichiometric mixture of Cu, In, and Te in an evacuated quartz ampule and then quenching in water. The obtained ingot was annealed at 823 K for 72 h, and then crushed into a fine powder. The powder was charged into pyrophyllite capsules and pressed at 5 GPa for 30 min in a high-pressure apparatus at room temperature. The typical size of the resultant polycrystalline samples was 4 mm in diameter and 3 mm thick. A typical preparation method was also used to produce reference samples, where the annealed ingot powder was hot-pressed in a graphite die under a pressure of 45 MPa at 823 K for 2 h in an Ar flow. The high-pressure-treated and hot-pressed polycrystalline samples, as a reference, are denoted as CIT-HP and CIT-R, respectively. Crushed powder samples were placed into a glass capillary tube for synchrotron X-ray diffraction (SXRD) measurements with a large Debye−Scherrer camera installed at the BL02B2 beamline of SPring-8. Rietveld refinement was performed using the RIETAN-FP program.[24] The wavelength used for the refinement was determined to be 0.500 575 Å using a CeO_2 standard. Microstrain was quantitatively evaluated by Williamson−Hall (W−H) analysis.[25] This analysis is a simplified method where both size-induced and strain-induced broadening is deconvoluted by considering the peak width as a function of 2θ, as expressed by the equation $\beta \cos \theta/\lambda = 2\varepsilon \sin \theta/\lambda + 0.9/D$, where β is half of the full width at half-maximum (fwhm) of the diffraction peak, θ is the diffraction angle, λ is the X-ray wavelength, ε is the strain, and D is the crystallite size. Nanoscale-domain structures in these polycrystalline samples were directly observed using transmission electron microscopy (TEM; Jeol, JEM-3010) operated at 300 kV. The bulk density was calculated on the basis of the weight and dimensions.

The thermoelectric properties ρ, S, and κ were measured from 2 to 300 K with a physical property measurement system (Quantum Design, PPMS). The room temperature κ value was also evaluated from the thermal diffusivity α, heat capacity C_p, and sample density d based on the relationship $\kappa = \alpha C_p d$. α and C_p were measured by the laser flash method and laser flash differential calorimetry in a vacuum (Picotherm, FlashTE).[26] The Hall coefficient R_H was measured at room temperature by the van der Pauw method in vacuum and under an applied magnetic field of 0.5 T. The carrier concentration n_H and the carrier mobility μ_H were calculated from R_H on the basis of the assumptions of a single-band model and a Hall factor of 1, that is, $n_H = 1/(eR_H)$ and $\mu_H = R_H/\rho$, where e is the elementary electric charge.

RESULTS AND DISCUSSION

Figure 1a shows SXRD patterns of CIT-R and CIT-HP, which are indexed as $CuInTe_2$ with the chalcopyrite structure, as previously reported.[27] No additional peaks were observed in the patterns of CIT-HP, which indicates that there are no structural changes and/or formation of additional phases within the SXRD detection limit. However, the peaks in the CIT-HP SXRD pattern are broader than those in the CIT-R pattern (Figure 1a, inset), which can be attributed to deviation from ideal crystallinity, such as finite crystallite size and strain at the atomic level, where strain is defined as the deviation of a lattice spacing divided by its ideal length ($\Delta d/d$). The broadening arises from vacancies, site disorder, dislocations, or even extended defects, and leads to systematic shifts of atoms from their ideal positions. Figure 1b shows the W−H analysis[25] of CIT-R and CIT-HP together with a CeO_2 standard sample. D was estimated from the y-intercept of the linear fit to the data, and ε from the slope of the fit. The slope of the linear fit for CIT-HP is larger than that for CIT-R, although CIT-R and CIT-HP have similar y-intercepts, which suggests that the room-temperature high-pressure synthesis induces strain in the $CuInTe_2$ matrix without changing the crystallite size (Table 1).

The nanoscale structures were directly observed to determine the origin of the strain induced in the high-pressure-treated $CuInTe_2$. A high-resolution transmission electron microscope (HRTEM) image (Figure 2a) along the

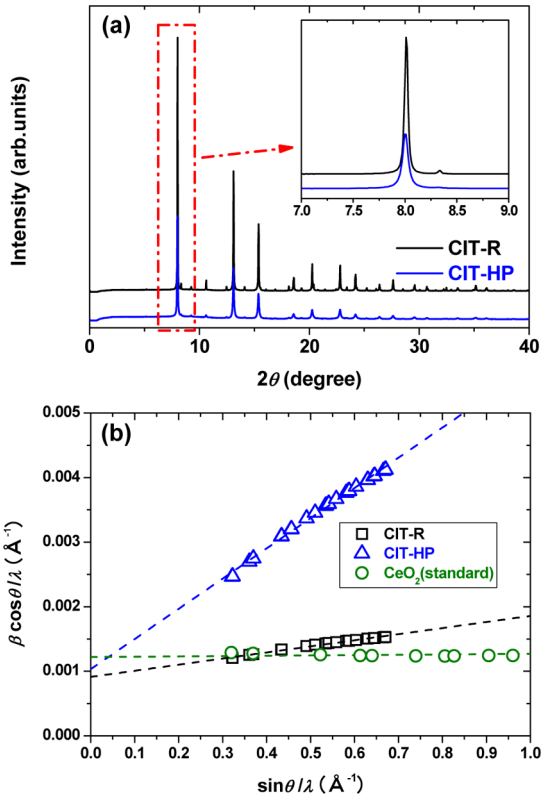

Figure 1. (a) SXRD patterns of CIT-R and CIT-HP. The intensity was normalized to the integrated intensity of the main peak for CIT-R and CIT-HP. (b) Williamson−Hall plots of CIT-R and CIT-HP, with CeO_2 as a reference.

Table 1. Comparison of the Structural Parameters of CIT-R and CIT-HP Refined from SXRD Data: The Tetragonal Lattice Parameters *a* and *c*, the Tetragonal Lattice Volume *V*, the Lattice Strain *ε*, and Crystallite Size *D*

	CIT-R	CIT-HP
Cu1 (4*a*)[c] g[a]	0.963(4)	0.801(4)
Cu1 (4*a*)[c] U (Å²)	0.0358(11)	0.0255(10)
In1 (4*a*)[c] g[a]	0.038	0.199
In1 (4*a*)[c] U (Å²)	0.0358(11)	0.0255(10)
In2 (4*b*)[c] g[a]	0.963(4)	0.801(4)
In2 (4*b*)[c] U (Å²)	0.0168(6)	0.0205(7)
Cu2 (4*b*)[c] g[a]	0.038	0.199
Cu2 (4*b*)[c] U (Å²)	0.0168(6)	0.0205(7)
Te (8*d*)[c] g[b]	1	1
Te (8*d*)[c] x	0.2235(17)	0.2276(18)
Te (8*d*)[c] U (Å²)	0.0151(3)	0.0135(3)
a (Å)[d]	6.19572(9)	6.1915(2)
c (Å)	12.4185(19)	12.4263(6)
V (Å³)	476.71(13)	476.36(3)
ε (%)	0.05	0.23
D (nm)	95	87

[a]Constraints used for the site occupancies g of the 4*a* and 4*b* sites: g(Cu1) + g(In1) = 1, g(In2) + g(Cu2) = 1, and g(In2) = g(Cu1). [b]g for Te was fixed at unity. [c]Atomic positions: Cu1 (In2) 4*a* (0, 0, 0); In2 (Cu2) 4*b* (0, 0, 1/2); and Te 8*d* (x, 1/4, 1/8). [d]The GOF and the R factors were GOF = 1.3305, R_{wp} = 5.079%, R_B = 4.038% for CIT-R, and GOF = 1.0868, R_{wp} = 2.193%, R_B = 0.733% for CIT-HP.

dx.doi.org/10.1021/ic500688d | Inorg. Chem. 2014, 53, 6844−6849

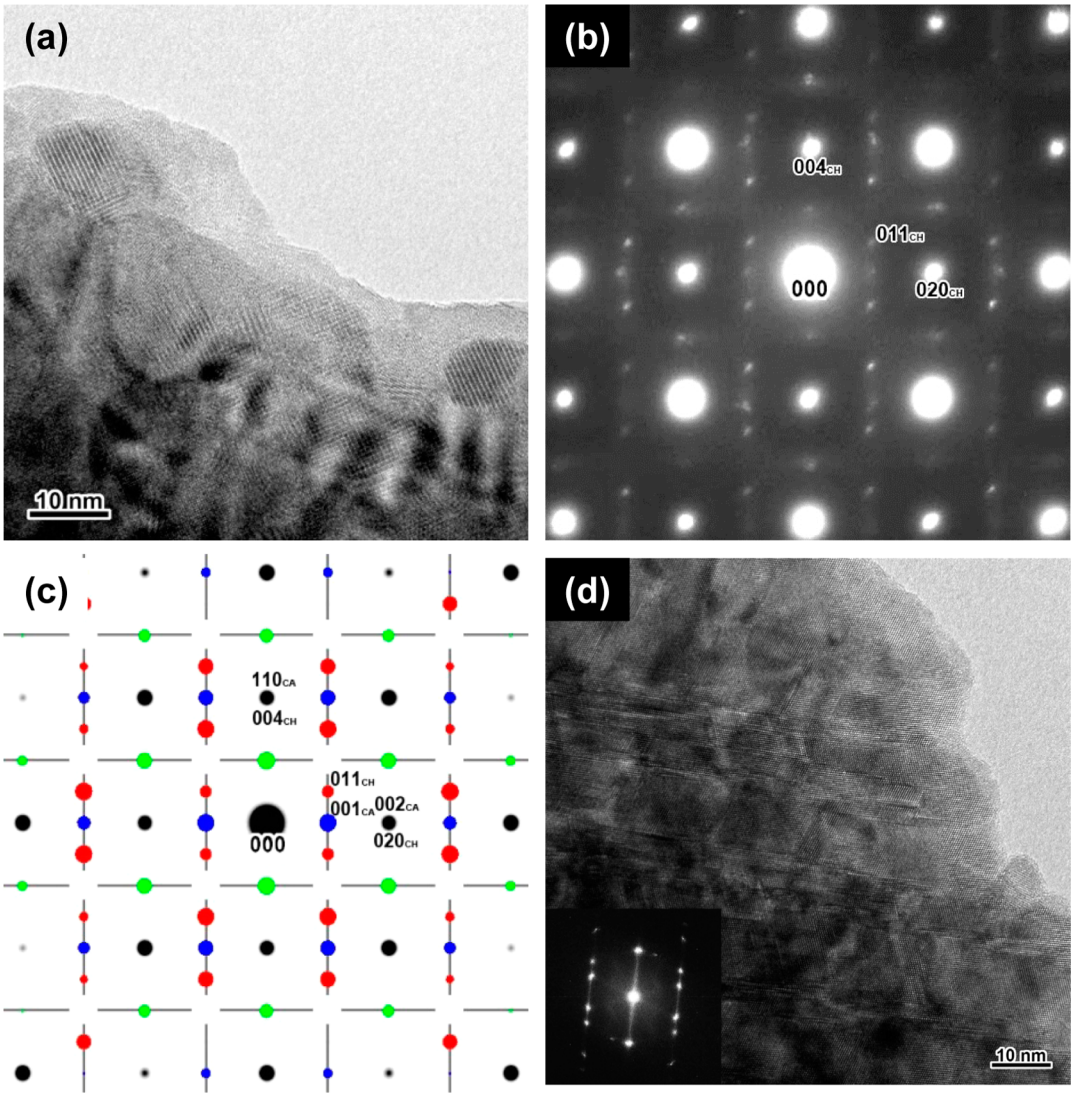

Figure 2. (a) HRTEM image of CIT-HP taken along the [100] direction of the chalcopyrite structure. (b) Corresponding ED pattern of part a, which indicates the coexistence of three distinct phases: chalcopyrite, disordered chalcopyrite, and CuAu-like structures. (c) Simulated ED pattern with fundamental reflections (black) of the three phases, superlattice reflections of the chalcopyrite (red) and CuAu-like structure (blue and green), and diffuse scattering of disordered chalcopyrite (black lines). (d) HRTEM image of CIT-HP with Fourier diffractogram. Many twin boundaries cause stacking faults in the structure.

$[100]_{CH}$ (CH represents the unit cell of the chalcopyrite structure) direction shows that the crystal grain of CIT-HP consists of domains with sizes of approximately a few tens of nanometers that have coherent crystallographic orientation relationships to one another. The $CuInTe_2$ system is composed of ternary I–III–VI_2 compounds that usually adopt the chalcopyrite structure (space group $I\bar{4}2d$) to form a $(Cu–Te)_2(In–Te)_2$ (201) superlattice.[28] The corresponding electron diffraction (ED) pattern (Figure 2b) of CIT-HP indicates the presence of three distinct phases with the same tetragonal lattice that give sharp fundamental reflections in the simulated ED pattern (black, Figure 2c). In contrast, the ordering of the two cations Cu and In gives superlattice reflections (chemically sensitive reflections). One is the chalcopyrite structure, in which the two cations Cu and In are ordered,[28] which leads to superlattice reflections such as $[011]_{CH}$, as shown by the reflections (red) in Figure 2c. The second is a CuAu-like structure (space group $P\bar{4}m2$), in which ordering of the cation sublattice planes along the $[001]_{CA}$ direction (CA represents the unit cell of the CuAu-like structure) is present as in a sphalerite analogue[29] with 001_{CA} reflections (blue and green) in Figure 2c. The blue and green ED reflections are rotated by 90°. The last is a disordered chalcopyrite structure with randomly distributed cations, as in a zinc blend analogue,[30] with diffuse scattering at the superlattice reflections of both chalcopyrite and CuAu-like structures, as shown by the black lines in Figure 2c. Further proof of the existence of the Cu–In disordered phase, which probably comes from disruption of the ordering of the chalcopyrite and CuAu-like structures, is shown in Figure S1 in the Supporting Information (SI). The characteristic features of each structure are shown in Figure S2 in the SI.

These results show that crystal grains of CIT-HP are composed of different types of domains with different degrees and geometries of site disorder at the Cu/In cation sites. Further refinement of the crystal structures of CIT-R and CIT-HP (see Figure S3, SI) was performed. A structural model with Cu and In antisite defects in definite proportions was assumed,

dx.doi.org/10.1021/ic500688d | Inorg. Chem. 2014, 53, 6844–6849

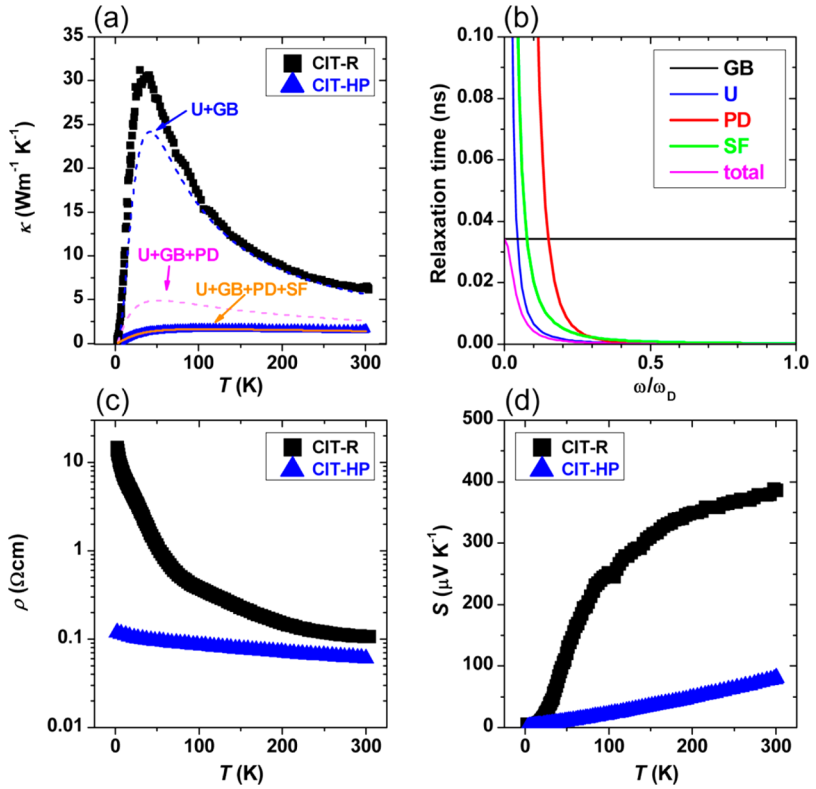

Figure 3. (a) Temperature dependence of κ for CIT-R and CIT-HP, together with κ_{lat} reduced by different processes: U, umklapp scattering; GB, grain boundary scattering; PD, point defect scattering; SF, stacking fault scattering. (b) Relaxation time versus normalized frequency of CIT-HP at 300 K. Temperature dependence of (c) the electrical resistivity ρ, and (d) the Seebeck coefficient S for CIT-R and CIT-HP.

and the Bragg R factor and goodness-of-fit (GOF) were smaller than for the Cu−In ordered model. The refined structural model indicated 19.9% replacement of Cu and In in CIT-HP, but only 3.8% in CIT-R (Table 1). In addition, the intensity of 101 peak in the Cu−In disordered model was weaker than that in the Cu−In ordered model, and a much better fit with the observed pattern of CIT-HP (see Figure S4, SI). Because the 101 peak corresponds to a superlattice reflection attributed to Cu−In ordering in the chalcopyrite structure, the intensity of the 101 peak gives further proof of Cu−In disorder in CIT-HP. Superlattice reflections of the CuAu-like structure were not confirmed in the SXRD, which is probably because of the low proportion of the CuAu-like structure in CIT-HP. Therefore, it is difficult to estimate the quantity of the CuAu-like structure in CIT-HP. As the CuAu-like structure was not observed in CIT-R using TEM, we believe that this structure was probably induced as a result of the room-temperature high-pressure treatment. Other structural parameters, such as the tetragonal lattice parameters and lattice volume, are also listed in Table 1. These results indicate antisite defects at the Cu/In cation sites are induced with pressure treatment, which causes strain in the sample. Another reason for the strain induced by pressure treatment could be stacking faults in the CIT-HP structure. Figure 2d shows a HRTEM image of CIT-HP with many stacking faults, which are typically observed as twins in the face centered cubic structure. $CuInTe_2$ has a c/a ratio of 2.014,[31] which is slightly different from 2.000. Therefore, the CIT-HP phase could form twin-type stacking faults under strain.

The temperature dependence of κ for CIT-R and CIT-HP is shown in Figure 3a. Note that there are no significant differences in the bulk densities (>97% of the theoretical density, see Table S1, SI) and microstructures (see Figure S5, SI), so the effects of pores and microstructures on the transport properties can be ignored. A very strong suppression of heat conduction was observed for CIT-HP at all temperatures. The κ values at about room temperature (290 K) were evaluated by two methods, the laser flash method (PicoTherm, Flash TE) and the steady-state method (Quantum Design, PPMS), and the two methods gave almost the same value (1.46 and 1.43 W m^{-1} K^{-1} at 290 K, respectively). In addition, we confirmed the reproducibility of low κ values in CIT-HP for several samples (see Figure S6, SI). κ_{lat} for CIT-R and CIT-HP was evaluated by subtracting the electronic contribution ($\kappa_{el} = LT\rho^{-1}$, where L is the Lorenz number: $L = 1.5 \times 10^{-8}$ W Ω K^{-2} for nondegenerate materials) from the measured κ value: $\kappa_{lat} = \kappa - \kappa_{el}$. The contribution of κ_{el} to the total κ value for CIT-R and CIT-HP was less than 10%, which is almost negligible within the temperature range examined. Therefore, phonon scattering dominates the heat conduction in this system. At room temperature, κ_{lat} for CIT-HP was 1.5 W m^{-1} K^{-1}, which is one-third that of CIT-R (4.5 W m^{-1} K^{-1}), but is still greater than the corresponding theoretical minimum thermal conductivity κ_{min} (0.35 W m^{-1} K^{-1} at room temperature) predicted by Cahill's theory:[32]

$$\kappa_{min} = \left(\frac{\pi}{6}\right)^{1/3} k_B n^{2/3} \sum_i v_i \left(\frac{T}{\Theta_D}\right)^2 \int_0^{\Theta_{D/T}} \frac{x^2 e^x}{(e^x - 1)^2} dx \quad (1)$$

where k_B is the Boltzmann constant, n is the number density of atoms, v is the average sound velocity, and θ_D is the Debye temperature (196 and 190 K for CIT-R and CIT-HP, respectively) estimated from the measurement of the low-

dx.doi.org/10.1021/ic500688d | Inorg. Chem. 2014, 53, 6844−6849

Table 2. Fitting Parameters of the Callaway Model for CIT-HP

	grain boundary, l (nm)	phonon umklapp, a	point defects, b	stacking faults, c
CIT-R	1500	1481	2.75×10^{-3}	
CIT-HP	680	836	4.75×10^{-2}	4.28×10^{-2}

temperature heat capacity in this study. v can be calculated from the relationship[33]

$$v = \frac{k_B \theta_D}{\hbar}\left(\frac{V}{6\pi^2}\right)^{1/3} \quad (2)$$

where $\hbar$ is the Plank constant and V is the atomic unit volume.

To understand the mechanism of phonon scattering in CIT-HP, a semiclassical theoretical calculation based on the Callaway model[34] was performed, where κ_{lat} is expressed as

$$\kappa_{lat} = \frac{k_B}{2\pi^2 v}\left(\frac{k_B T}{\hbar}\right)^3 \int_0^{\theta_D/T} \frac{\tau_c e^x x^4}{(e^x - 1)^2}\, dx \quad (3)$$

where x is defined as $\hbar\omega/k_B T$, ω is the onon frequency, and τ_c is a combined term of the phonon scattering relaxation time. The following processes are assumed to limit the flow of phonons: scattering from grain boundaries (τ_B),[35] umklapp scattering (τ_U),[35] point defects (τ_{PD}),[35] and stacking faults (τ_S).[36]

$$\tau_c^{-1} = \tau_B^{-1} + \tau_U^{-1} + \tau_{PD}^{-1} + \tau_S^{-1} = v/l + a(\hbar\gamma^2/Mv^2\theta)\omega^2 T e^{\vartheta/3T} + b(V/4\pi v^3)\omega^4 + c(2\gamma^2 V^{1/3}/27v)\omega^2 \quad (4)$$

Here, l is the typical grain size, and a, b, and c are fitting parameters for scattering from phonon−phonon umklapp, point defects, and stacking faults, respectively. γ, M, and V represent the Grüneisen constant, average volume per atom, and average mass per atom, respectively, and were fixed for the calculation. The value of $\gamma = 2.2$ was taken from ref 37. No evidence of stacking faults was evident in CIT-R, so c was set at 0 for CIT-R.

The fitting parameters are given in Table 2, and fits to the κ_{lat} data are shown in Figure 3a, together with the simulated κ_{lat} data reduced by different scattering processes. Table 2 indicates that the a and c parameters of CIT-HP are significantly less than those of CIT-R. In our analysis, scattering from point defects and stacking faults was dominant around room temperature, while scattering from grain boundaries was greater in the low temperature range (Figure 3a). Figure 3b shows the corresponding frequency-dependent relaxation times for each phonon scattering mechanism at 300 K normalized according to the Debye frequency. The results indicate that point defects scatter phonons with high frequency, while grain boundary scattering plays an important role at low frequency. Phonons with medium frequency were scattered by stacking faults. Thus, phonons with a wide range of frequency were scattered by different defects.

The temperature dependence of ρ and S is shown in Figure 3c,d, respectively. ρ of CIT-R rapidly decreased with increasing temperature over the entire temperature range. S of CIT-R increased to approximately 400 μV K^{-1} at 300 K. The temperature dependence of the transport properties of CIT-R is similar to that for a lightly doped semiconductor. In contrast, especially below room temperature, ρ of the CIT-HP system is 1 order of magnitude lower than that for CIT-R, and exhibits rather weak temperature dependence up to ca. 300 K. In addition, S of CIT-HP is lower than that of CIT-R within the temperature range examined. Thus, the CIT-HP system appears to behave similarly to a heavily doped semiconductor, which is supported by the n_H measurements. The n_H of CIT-HP at room temperature was 2.2×10^{19} cm^{-2}, which is 2 orders of magnitude higher than that of CIT-R (4.3×10^{17} cm^{-2}). The cation site disordered chalcopyrite has a smaller energy gap than that in ordered chalcopyrite.[30] Therefore, the low ρ in CIT-HP can be attributed to decrease of the band gap caused by antisite defects. However, the μ_H of CIT-HP at room temperature (4.9 cm^2 V s^{-1}) was significantly less than that of CIT-R (111 cm^2 V s^{-1}), which is probably because of enhanced carrier scattering at the Cu/In cation site defects and stacking faults.

The large decrease in κ was compensated for by a decrease in the power factor $S^2\rho^{-1}$ in CIT-HP. Thus, no enhancement of ZT of CIT-HP was achieved in this study. Although we were not able to optimize the thermoelectric properties, the improvement of ZT using room-temperature high-pressure synthesis is possible, if we can combine room-temperature high-pressure synthesis (to generate defects) with doping (to adjust carrier concentration). One of the advantages of this preparation method is that the atomic-scale replacement occurs even at room temperature. It has been reported that the normal chalcopyrite structure is transformed to the disordered structure at around 950 K.[30] However, thermogravimetry−differential thermal analysis (TG−DTA) indicated that mass loss began at around 700 K, probably because of the evaporation of tellurium (see Figure S7, SI). Therefore, it is difficult to maintain the stoichiometric composition of $CuInTe_2$ with the disordered chalcopyrite structure by heat treatment. Thus, this method is an alternative for the fabrication of chalcopyrite compounds including disorder with the compositional stoichiometry maintained. The next issue is to clarify the reason for the evolution of multiple nanoscale domains in the thermoelectric $CuInTe_2$ matrix. There are a number of possible kinetic and thermodynamic mechanisms that can produce multiple nanoscale domains. For example, the temperature−pressure phase diagram has yet to be clarified, and there could be a miscibility gap between the chalcopyrite phase and d-*Cmcm* phase. In this case, the high-pressure-treated phase may be a metastable phase in the miscibility gap, which can allow us to separately control the degree and proportion of the different scales of disorder, from antisite defects to nanoscale domain disorder, by means of the pressure intensity and the pressure application and release rates, leading to a potential enhancement of ZT. Theoretical calculations of the formation energies of different ordered chalcopyrite structures are necessary to explore the driving force for the coexistence of multiple nanoscale domain structures.

CONCLUSION

In summary, nanostructured thermoelectric $CuInTe_2$ bulk material was successfully fabricated by room-temperature high-pressure synthesis. The high-pressure-treated $CuInTe_2$ contains distinct domains with various degrees and geometries of disorder at the Cu/In cation sites and stacking faults between domains, which causes strain in the sample as a whole. The

dx.doi.org/10.1021/ic500688d | Inorg. Chem. 2014, 53, 6844−6849

thermal conductivity of high-pressure-treated $CuInTe_2$ was substantially less than that of the hot-pressed $CuInTe_2$, probably because of enhanced phonon scattering of antisite disorder and stacking faults created during the pressure treatment. Although a large reduction in the thermal conductivity of high-pressure-treated $CuInTe_2$ was compensated for by a decrease in the power factor, room-temperature high-pressure synthesis could be an alternative method to tune the thermoelectric properties of chalcopyrite compounds. Moreover, room-temperature high-pressure synthesis could be a novel method to produce conventional inorganic materials with unusual and useful properties that are different from those of either the pre-pressure-treated or high-pressure phase.

■ ASSOCIATED CONTENT

Supporting Information

Additional figures for the electron diffraction pattern and the Fourier diffractogram of different CIT-HP crystals from Figure 2b, the crystal structures existing in CIT-HP, Rietveld refinement results for CIT-R and CIT-HP, enlarged images of the (101) peak of CIT-HP for comparison of the refinements between the Cu−In ordered and Cu−In disordered models, scanning electron microscope images of CIT-R and CIT-HP, temperature dependence of κ for several samples of CIT-R and CIT-HP, and TG−DTA profile for CIT-R. This material is available free of charge via the Internet at http://pubs.acs.org.

■ AUTHOR INFORMATION

Corresponding Author

*E-mail: a-kosuga@21c.osakafu-u.ac.jp.

Author Contributions

The manuscript was written through contributions of all authors. All authors have given approval to the final version of the manuscript.

Notes

The authors declare no competing financial interest.

■ ACKNOWLEDGMENTS

This work was supported by a Grant-in-Aid for Young Scientists (B) (No. 25870626) and the Special Coordination Funds for Promoting Science and Technology from the Ministry of Education, Culture, Sports, Science and Technology of Japan (MEXT) (Improvement of Research Environment for Young Researchers). The synchrotron radiation experiments were performed at SPring-8 with the approval of the Japan Synchrotron Radiation Research Institute (JASRI, Proposal No. 20131043, and JAEA, Proposal No. 2012B3622). A.K. acknowledges Dr. R. Funahashi for use of the high-temperature thermal conductivity apparatus.

■ REFERENCES

(1) Wang, Y. M.; Ma, E. *Acta Mater.* **2004**, *52*, 1699−1709.
(2) Minnich, A. J.; Dresselhaus, M. S.; Ren, Z. F.; Chen, G. *Energy Environ. Sci.* **2009**, *2*, 466−479.
(3) Nishizaki, T.; Lee, S.; Horita, Z.; Sasaki, T.; Kobayashi, N. *Physica C* **2013**, *493*, 132−135.
(4) Tritt, T. M.; Subramanian, M. A. *MRS Bull.* **2006**, *31*, 188−198.
(5) Pei, Y.; Lensch-Falk, J.; Toberer, E. S.; Medlin, D. L.; Snyder, G. J. *Adv. Funct. Mater.* **2011**, *21*, 241−249.
(6) Lo, S.-H.; He, J.; Biswas, K.; Kanatzidis, M. G.; Dravid, V. P. *Adv. Funct. Mater.* **2012**, *22*, 5175−5184.
(7) He, J.; Girard, S. N.; Zheng, J. C.; Zhao, L.; Kanatzidis, M. G.; Dravid, V. P. *Adv. Mater.* **2012**, *24*, 4440−4444.
(8) Androulakis, J.; Lin, C. H.; Kong, H. J.; Uher, C.; Wu, C. I.; Hogan, T.; Cook, B. A.; Caillat, T.; Paraskevopoulos, K. M.; Kanatzidis, M. G. *J. Am. Chem. Soc.* **2007**, *129*, 9780−9788.
(9) Rogl, G.; Grytsiv, A.; Rogl, P.; Royanian, E.; Bauer, E.; Horky, J.; Setman, D.; Shafler, E.; Zehetbauer, M. *Acta Mater.* **2013**, *61*, 6778−6789.
(10) Rogl, G.; Rogl, P.; Bauer, R.; Zehetbauer, M.. *Thermoelectric Nanomaterials*; Springer: Heidelberg, 2013.
(11) Mori, Y.; Ikai, T.; Takarabe, K. *Phys. Status Solidi* **2003**, *235*, 317−320.
(12) Iwamoto, S.; Mori, Y.; Takarabe, K.; Minomura, S. *Rev. High Pressure Sci. Technol.* **1998**, *7*, 327−328.
(13) Range, K.-J.; Engert, G.; Weiss, A. *Solid State Commun.* **1969**, *7*, 1749−1752.
(14) Kosuga, A.; Plirdpring, T.; Higashine, R.; Matsuzawa, M.; Kurosaki, K.; Yamanaka, S. *Appl. Phys. Lett.* **2012**, *100*, 042108.
(15) Liu, R.; Xi, L.; Liu, H.; Shi, X.; Zhang, W.; Chen, L. *Chem. Commun.* **2012**, *48*, 3818−3820.
(16) Plirdpring, T.; Kurosaki, K.; Kosuga, A.; Day, T.; Firdosy, S.; Ravi, V.; Snyder, G. J.; Harnwunggmoung, A.; Sugahara, T.; Ohishi, Y.; Muta, H.; Yamanaka, S. *Adv. Mater.* **2012**, *27*, 3622−3626.
(17) Yusufu, A.; Kurosaki, K.; Kosuga, A.; Sugahara, T.; Muta, H.; Yamanaka, S. *Appl. Phys. Lett.* **2011**, *99*, 061902.
(18) Tsujii, N.; Mori, T. *Appl. Phys. Express* **2013**, *6*, 043001.
(19) Parker, D.; Singh, D. J. *Phys. Rev. B* **2012**, *85*, 125209.
(20) Zhang, J.; Xu, B.; Wang, L.-M.; Yu, D.; Liu, Z.; He, J.; Tian, Y. *Appl. Phys. Lett.* **2011**, *98*, 072109.
(21) Yamada, I.; Tsuchida, K.; Ohgushi, K.; Hayashi, N.; Kin, J.; Tsuji, N.; Takahashi, R.; Matsushita, M.; Nishiyama, N.; Inoue, T.; Irifune, T.; Kato, K.; Takata, M.; Takano, M. *Angew. Chem., Int. Ed.* **2011**, *50*, 6579−6582.
(22) Meng, J. F.; Polvani, D. A.; Jones, C. D. W.; DiSalvo, F. J.; Fei, Y.; Badding, J. V. *Chem. Mater.* **2000**, *12*, 197−201.
(23) Ovsyannikov, S. V.; Shchennikov, V. V. *Chem. Mater.* **2010**, *22*, 635−647.
(24) Izumi, F.; Momma, K. *Solid State Phenom.* **2007**, *130*, 15−20.
(25) Williamson, G. K.; Hall, W. H. *Acta Metall.* **1953**, *1*, 22−31.
(26) Shinzato, K.; Baba, T. *J. Therm. Anal. Calorim.* **2001**, *64*, 413−422.
(27) Grzeta-Plenkovic, B.; Santic, B. *J. Appl. Crystallogr.* **1983**, *16*, 576.
(28) Chen, S.; Gong, X. G. *Phys. Rev. B* **2009**, *79*, 165211.
(29) Su, D. S.; Neumann, W.; Hunger, R.; Schubert-Bischoff, P.; Giersig, M.; Lewerenz, H. J.; Scheer, R.; Zeitler, E. *Appl. Phys. Lett.* **1998**, *73*, 785−787.
(30) Rincón, C. *Phys. Rev. B* **1992**, *45*, 12716−12719.
(31) Knight, K. S. *Mater. Res. Bull.* **1992**, *27*, 161−167.
(32) Cahill, D. G.; Watson, S. K.; Pohl, R. O. *Phys. Rev. B* **1992**, *46*, 6131−6140.
(33) Steigmeier, E. F.; Abeles, B. *Phys. Rev.* **1964**, *136*, A1149−A1155.
(34) Callaway, J. *Phys. Rev.* **1959**, *113*, 1046−1051.
(35) Morelli, D. T.; Heremans, J. P.; Slack, G. A. *Phys. Rev. B* **2002**, *66*, 195304.
(36) Klemens, P. *Can. J. Phys.* **1957**, *35*, 441−450.
(37) Copper indium telluride ($CuInTe_2$). *Ternary Compounds, Organic Semiconductors*; Ditrich, H., Karl, N., KückS., Schock, H. W., Madelung, O., Eds.; Springer: New York, 2000.